Microfluidics and Spectral Induced Polarization for Direct Observation and Petrophysical Modeling of Calcite Dissolution

F. Rembert, P. Leroy, A. Lassin, S. Roman

AGU ADVANCING EARTH AND SPACE SCIENCES

Geophysical Research Letters

RESEARCH LETTER
10.1029/2024GL111271

Key Points:

- Microfluidics enables direct visualization of pore scale reactive transport and determining petrophysical parameters from image processing
- Combining microfluidics with geoelectrical monitoring enables upscaling of pore scale observations
- Petrophysical modeling applies to pore scale geoelectrical monitoring

Supporting Information:

Supporting Information may be found in the online version of this article.

Correspondence to:

F. Rembert,
flore.rembert@ugent.be

Citation:

Rembert, F., Leroy, P., Lassin, A., & Roman, S. (2024). Microfluidics and spectral induced polarization for direct observation and petrophysical modeling of calcite dissolution. *Geophysical Research Letters*, *51*, e2024GL111271. https://doi.org/10.1029/2024GL111271

Received 12 JUL 2024
Accepted 25 OCT 2024

Author Contributions:

Conceptualization: F. Rembert, P. Leroy, A. Lassin, S. Roman
Data curation: F. Rembert, A. Lassin, S. Roman
Formal analysis: F. Rembert
Funding acquisition: F. Rembert, S. Roman
Investigation: F. Rembert
Methodology: F. Rembert, P. Leroy, A. Lassin, S. Roman
Project administration: F. Rembert, S. Roman
Resources: F. Rembert, S. Roman
Software: F. Rembert, P. Leroy, A. Lassin, S. Roman
Supervision: S. Roman
Validation: F. Rembert, A. Lassin

Microfluidics and Spectral Induced Polarization for Direct Observation and Petrophysical Modeling of Calcite Dissolution

F. Rembert[1], P. Leroy[2], A. Lassin[2], and S. Roman[1]

[1]Univ. Orléans, CNRS, BRGM, ISTO, UMR, Orléans, France, [2]BRGM, French geological survey, Orléans, France

Abstract We investigate how micro-geoelectrical monitoring is promising for studying microscale coupled processes since it facilitates the upscaling of pore-scale observations and enhances the petrophysical interpretation of the geoelectrical measurements. Microscale geophysics using microfluidics emerges and combines direct visualization of pore scale dynamics and chemical reactivity with geoelectrical monitoring. Calcite dissolution is a usual geochemical reaction considered as an analog of water–mineral interactions involved in the critical zone. We develop a numerical workflow combining image processing and geochemical simulation as inputs for the petrophysical modeling applied to a published data set of microscale induced polarization monitoring of calcite dissolution under partially saturated conditions. The successful interpretation provides the cation exchange capacity and specific surface area evolution; essential parameters in field-scale surveys.

Plain Language Summary Surface and borehole geoelectrical prospecting is used to understand the structure of the subsurface and the functioning of the processes that take place there. These processes include flows and changes in groundwater stocks, transport of pollutants, and dissolution and precipitation of minerals. The complexity of studying these processes lies in the large-scale impact that arises from mechanisms and interactions occurring at the microscopic scale. In addition, the complexity of the heterogeneous natural environment makes it difficult to interpret the measurements obtained on-site. Pore-scale experimental studies reveal a refined understanding of these processes. In particular, microfluidics for geosciences uses optical microscopy to visualize flow, transport, and reactive processes. This approach demonstrates the natural heterogeneity of processes in porous media, even at the pore scale, and how the electrical signal measured on the investigated volume accounts for the average behavior of these processes. Studies at the micrometric scale are questioned for their representativeness compared to related field-scale applications. In this study, we validate the link between scales through a conceptual model widely used for field-scale prospecting and show that the geoelectrical response remains sensitive to the same couplings.

1. Introduction

Microfluidics in geosciences enables direct visualization of flows, chemical reactions, and particle transport at the pore scale thanks to transparent micromodels coupled with optical microscopy and high-resolution imaging techniques (Roman et al., 2016). Micromodels are a two-dimensional representation of the porous medium, ranging in complexity from single channels to replicas of natural rocks (Soulaine & Roman, 2022; Yun et al., 2017). Cutting-edge micromodels use reactive minerals to investigate hydrogeochemical processes (Osselin et al., 2016; Poonoosamy et al., 2020). For example, calcite dissolution is a process that has recently drawn attention in microfluidics (Rembert, Stolz, et al., 2023; Song et al., 2014; Soulaine et al., 2017, 2018). Two-phase flow in the confined porous matrix is also an important topic, where microfluidic observations lead to new theoretical findings (e.g., viscous dissipation, Haines jumps) about fluid interactions (e.g., water, oil, supercritical carbon dioxide) in the porous matrix, influencing the reservoir sequestration or recovery capacities (Mansouri-Boroujeni et al., 2023; Riazi et al., 2011; Roman et al., 2020). Microfluidic studies give a very detailed description of the heterogeneity and dynamics of the processes happening at the pore scale. Pore-scale mechanisms investigated by microfluidics explain many macroscopic observations regarding reactive and dynamic processes (e.g., clogging, weathering, wettability alteration) and are recently considered in numerical models (H. Li et al., 2023; Norouzisadeh et al., 2024; Soulaine, 2024). However, there is still an issue related to microfluidics for large-scale

Visualization: F. Rembert
Writing – original draft: F. Rembert
Writing – review & editing: F. Rembert, P. Leroy, A. Lassin, S. Roman

studies. Therefore, coupling microfluidics with integrative monitoring methods is essential for characterization across scales.

Geoelectrical prospecting gives a non-intrusive and real-time characterization of the structure of the subsurface and the hydrogeological and geochemical processes occurring therein since they are sensitive to the presence of water, pollutants (e.g., heavy metals, hydrocarbons), and air, as well as to the mineralogy and structure of the rock matrix (Rahmani et al., 2024; Rembert et al., 2020; Rembert, Léger, et al., 2023; Revil et al., 2012). Recently, coupled with geochemical simulation, geoelectric signals for multiphase reactive systems are better understood and quantified (Rembert et al., 2022). Geochemical simulation provides information on the chemical composition within the pore space, which serves to calculate the electrical conductivity of the electrolyte in the channel, an input parameter for petrophysical modeling. Among the geoelectrical methods, the spectral induced polarization (SIP) measures the complex electrical conductivity $\sigma^* = \sigma' + i\sigma''$ (S m^{-1}), a physical property directly influenced by lithology, rock structure, water content and chemistry, and mineral surface state (Bate et al., 2021; Ben Moshe et al., 2021). It measures both the electrical conduction (σ') and the interfacial polarization (σ'') in a porous medium (Binley & Kemna, 2005; Binley & Slater, 2020; Kemna et al., 2012; Revil & Florsch, 2010).

Calcite dissolution is considered in the literature to create conditions not suitable for measurable SIP variations at the macroscale (Halisch et al., 2018). However, monitoring this physical property at the microscale to characterize the dissolution of a calcite grain has been performed for the first time by Rembert, Stolz, et al. (2023). The authors have shown that comparing the optical images with the electrical signal enables a better understanding of the SIP time variations. There is a significant interest in using petrophysical modeling to interpret SIP measurements by Rembert, Stolz, et al. (2023) at the pore scale. The objective is to determine whether the findings at the microscale can be interpreted for dynamic interactions and reactive processes field investigations using generic petrophysical modeling from the geophysical community.

Equivalent circuit modeling (Waxman & Smits, 1968) is investigated. It conceptualizes the porous medium as resistors and capacitors put on serial and parallel connections to consider conduction and polarization processes. The electric circuit components integrate and interpret the bulk electrolyte and the electrical double layer (EDL) contributions to the complex conductivity response of the porous medium. The EDL compensates for the usually negative surface charge of the mineral when in contact with water and is commonly composed of the highly viscous Stern layer containing mostly counter-ions (i.e., cations) and the diffuse layer containing counter-ions in the majority and co-ions (i.e., anions) in the minority (Revil & Florsch, 2010). The famous Cole-Cole model and Pelton equation are based on such a description (Tarasov & Titov, 2013) and include the frequency effect. Only single-frequency models consider partially saturated conditions (Laloy et al., 2011; Vinegar & Waxman, 1984). However, forward petrophysical models in SIP require input parameters such as porosity, water content, and bulk water conductivity (Koohbor et al., 2022). These parameters can be estimated from reactive transport modeling and optical microscopy measurements (Soulaine et al., 2018). Thus, this study is based on developing a workflow that combines image processing and geochemical simulation with petrophysical modeling to provide this information in a complementary manner.

The manuscript is divided into two parts. First, the Materials and Methods section, which summarizes the experimental setup for the microfluidics experiment of calcite dissolution monitored with SIP and microscope images published by Rembert, Stolz, et al. (2023), introduces the workflow of the developed modeling approach, and presents the serial steps corresponding to image processing, geochemical simulation, and petrophysical modeling. Second, the measurements of the time variations of SIP measurements of a single frequency and the associated modeling results are presented and discussed.

2. Materials and Methods

2.1. Experimental Setup

This study presents the first petrophysical modeling of microscale SIP monitoring. The experimental data come from the study of Rembert, Stolz, et al. (2023), the only one of its kind, which focuses on the manufacturing of the micromodel and was published in a journal specialized in microfluidics design developments, which is not a primary source for the geophysical community. Thus, we briefly summarize the specifications of the setup which is presented in Figure 1. The microfluidic chip is mounted on the translation stage of an upright microscope (Nikon, Eclipse Ni) and connected to the PSIP instrument (Portable SIP from Ontash&Ermac, see Figure 1a). The

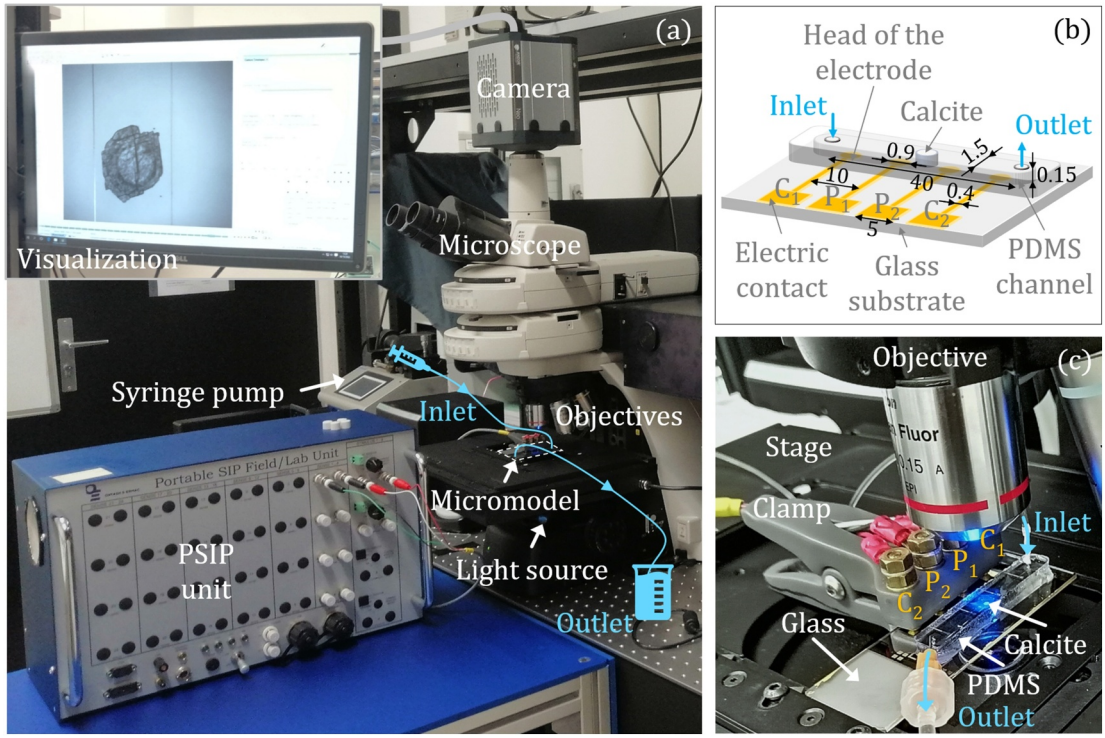

Figure 1. (a) The setup. (b) The design of the micromodel (dimensions in mm). (c) The micromodel. The 3D-printed clamp maintains the connection with the electrodes.

micromodel is a straight channel (L × l × h = 4000 × 1500 × 150 μm) molded in a soft silicone material (polydimethylsiloxane, PDMS). PDMS is a well-documented material, extensively used for microfluidics, not sensitive to aqueous solvents (Lee et al., 2003), and suitable for multi-phase flow experiments. The PDMS channel is bonded on a glass substrate on which four gold electrodes are printed (Figure 1b). Each electrode consists of a round head (900 μm diameter) in contact with the electrolyte in the channel and electrical contacts (500 μm^2 area), deported aside from the channel through a thin trace (400 μm width). The Wenner-α configuration usually considered in laboratory and field geophysical samples is used for the SIP acquisition (Zarif et al., 2017). In this configuration, the electrodes are equally spaced (inter-electrode distance of 1,000 μm) to avoid their interaction, and the pair of electrodes for the potential measurement (P_1 and P_2) is between the pair of electrodes for current injection (C_1 and C_2). The electrical wires of the PSIP unit are connected to the electrical contacts of the micromodel by a 3D-printed clamp with screws pressing against the printed contacts of the electrodes (Figure 1c). The SIP response is monitored continuously during the entire dissolution process on the frequency range from 1 Hz to 10 kHz, with a stimulus voltage of ±1 V, and a reference resistor of 1MΩ.

A calcite grain of 150 μm thickness and 1 mm diameter is sandwiched in the middle of the microfluidic channel. In this configuration, the flow is channeled around the grain, not over or under. The camera (Andor, Neo) mounted on the microscope captures the top view of the channel using magnification ×5. Figure 1a shows the calcite grain in the channel on the computer screen. The channel is initially saturated with an aqueous solution prepared in advance so that the geochemical conditions reflect equilibrium with calcite. This solution is named S_0 and has an electrical conductivity $\sigma_{S_0} = 0.01$ S m^{-1}. Under atmospheric pressure and ambient temperature conditions, an aqueous solution composed of 0.05 wt.% chloride acid (HCl) is injected into the microfluidic channel with a constant flow rate of 1.25 mL hr^{-1} using a syringe pump. The acid solution has a conductivity $\sigma_{HCl} = 0.44$ S m^{-1}. Working at atmospheric pressure, a two-phase flow is generated by carbon dioxide (CO_2) bubbles production during dissolution. The calcite sample is fully dissolved in 4.29 hr.

2.2. Modeling Approach

Petrophysical, hydrological, and geochemical parameters are necessary to resolve the petrophysical modeling. Thus, a modeling workflow is developed and comprises a coupled approach combining image processing,

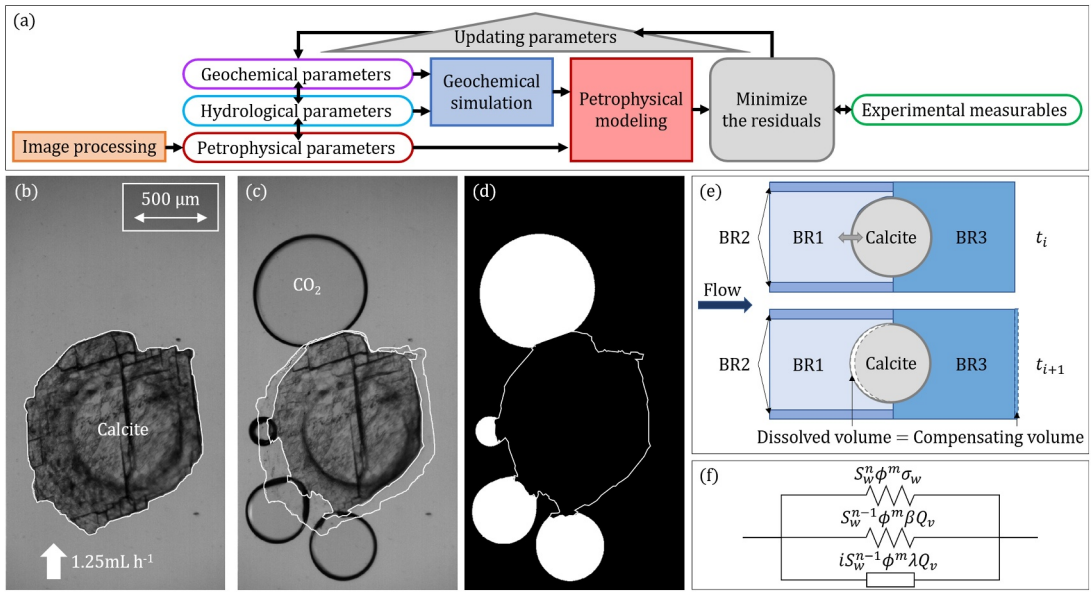

Figure 2. (a) Workflow for the petrophysical modeling coupled with image processing and geochemical modeling to set the input parameters and help minimize the residuals (b–d) Images from the microscope acquisition and their processing. (b) The calcite sample at the beginning of the experiment with initial calcite contour in white. (c) The dissolving calcite sample at time $t = 0.72$ hr with initial and actual calcite contours in white. (d) The image segmentation displays the bubbles and calcite contour in white. (e) Sketch of the reactive pseudo-transport modeling. (f) Electrical complex conductivity equivalent circuit model.

hydrological, and geochemical modeling to set input parameters for the petrophysical modeling (Figure 2a). Image processing informs on porosity and water saturation. Hydrological and geochemical modeling input parameters come from the experimental conditions. The geochemical modeling informs on the water conductivity, pH, and porosity. Porosity obtained from image processing and geochemical modeling are compared to ensure consistency. This type of workflow is inspired from (e.g., Rembert et al., 2022), but every processing and modeling is designed for this study and is not published elsewhere.

2.3. Image Processing

The calcite sample grayscale image sequence is obtained from the microscope observations (Figures 2b–2d). Initially, the calcite sample presents a sharp-edged contour in fully saturated conditions (Figure 2b). Figures 2c and 2d show the simultaneous grayscale and segmented images of the dissolving calcite sample surrounded by CO_2 bubbles, respectively. Image processing is performed using Matlab codes (Soulaine et al., 2018). Image segmentation is performed to track the contour of the calcite grain and bubbles in the observation window. All of the interpretation is based on a 2D approximation of the system and enables determining the base area A_{CaCO_3} (m^2), perimeter of the calcite sample P_{CaCO_3} (m), and area of the bubbles A_{CO_2} (m^2). Then, knowing the thickness of the channel h (m), the volumes of calcite $V_{CaCO_3} = h\,A_{CaCO_3}$ (m^3) and CO_2 bubbles $V_{CO_2} = h\,A_{CO_2}$ (m^3) are retrieved. This supposes that bubbles are not spherical but cylindrical due to the 2D approximation made using the thin micromodel. From these volumes, we determine the porosity ϕ (−), water content θ (−), water saturation S_w (−), and specific surface area S_s ($m^2\ kg^{-1}$) as follows,

$$\phi = \frac{V_{\text{pores}}}{V} = \frac{V - V_{CaCO_3}}{V}, \tag{1}$$

$$\theta = \frac{V_w}{V} = \frac{V - V_{CaCO_3} - V_{CO_2}}{V}, \tag{2}$$

$$S_w = \frac{\theta}{\phi}, \tag{3}$$

$$S_s = \frac{h\, P_{CaCO_3}}{V_{CaCO_3}\, \rho}, \quad (4)$$

where V (m^3) is the channel volume in the observation window, V_w (m^3) is the water volume in the observation window, and $\rho = 2710$ kg m^{-3} is the volumetric density of the calcite grain (Leroy, Li, et al., 2017). The volume V corresponds to the volume on which the electrical response is integrated. Porosity and water saturation time variations are inputs for the complex electrical conductivity modeling.

2.4. Geochemical Simulation

We use a simplified mass transfer model to fulfill the workflow objectives and the petrophysical description of the system. The idea of the geochemical simulation is to achieve a good compromise between the information required for the petrophysical model and the complexity of its implementation. To achieve this, we schematically distinguish different water compartments (batch reactors, BR): pre-reaction BR1, non-reactive BR2, and post-reaction BR3 (Figure 2e), to simulate a simplified transport. We call it pseudo-transport to simulate mass transfer as an open batch system. The three batch reactors are connected following a specific time sequence. The first batch reactor BR1 represents the upstream acid solution that arrives in the pore volume and reacts with calcite. Assuming laminar flow, the second batch reactor BR2 represents the upstream acidic solution that passes on the sides of the calcite without reaction. The third batch reactor BR3 represents the downstream part, where BR1 and BR2 mix with the solution remaining in BR3 after the previous time step and without further interaction with calcite. Thus, transport is simulated by successive mixing, with partial replacement of a batch solution by the inlet solution. This principle is similar to what underlies 1D reactive-transport modeling (Parkhurst & Appelo, 2013), a succession of individual perfectly mixed batches. This open batch simulation allows distinguishing a proportion of non-reactive water close to the pore walls and considering the liquid-solid ratio variation in a constant cell volume while calcite dissolves. It is, therefore, a compromise between 1D transport model, where the non-reactive compartment cannot be distinguished, and the more complex 2D transport model.

We ran the simulation using PhreeqC v3 software (Parkhurst & Appelo, 2013) and the thermodynamic database Thermoddem (Blanc et al., 2012). The initial geometry of the simulated system and the injection conditions exactly mimic the microfluidic experiment, with a pore volume between the measuring electrodes of 6.39 μL, the initial calcite volume of 2.61 μL, and the flow rate of 20.83 μL min^{-1}. According to the pore volume and the flow rate, the solution is renewed every 0.307 min (≈18.4s). Therefore, a time step of 10s is considered to simulate its partial replacement (c.a., 54.34% of the initial pore volume) and interaction with calcite. For each time step of 10s, a volume of 3.47 μL of the acid solution fills reservoirs BR1 and BR2 (Figure 2e). To maintain a constant total volume, the same volume of the solution initially present is removed. According to the configuration of the calcite sample in the channel, it is assumed that a certain percentage of the injected solution does not react (reservoir BR2). Different volume fractions have been tested and the resulting estimated one is 5%. This value has been determined from the best retrieval of the porosity and water conductivity measurements. Thus, 95% of the injected solution (volume of BR1) reacts with calcite. The reaction is assumed to occur instantaneously, or fast enough to reach thermodynamic equilibrium in 10 (Damköhler and Péclet numbers presented in Supporting Information S1 validate this). The volume of the solution mixture in BR3 is reduced to account for the amount of calcite that dissolves at each time step.

The simulation intends to correspond to the results obtained at full water saturation and does not reproduce bubble formation. The simulation is thus run for 780 (i.e., 13 min) in 80 steps, before the nucleation of the first bubbles. Since the water conductivity value is needed for the entire experiment, after 13 min of dissolution, the variation of the water conductivity is assumed to continuously increasing linearly with time and reaching the value of the injected acid solution after the complete dissolution of the calcite grain.

2.5. Petrophysical Modeling

Based on equivalent circuit modeling (Figures 2f) and Waxman and Smits (1968) have proposed expressions for the components of the complex electrical conductivity that have been extended to partially saturated conditions by Vinegar and Waxman (1984) as follows

$$\sigma' = \phi^m S_w^n \left(\sigma_w + \frac{\beta Q_v}{S_w}\right), \tag{5}$$

$$\sigma'' = \phi^m S_w^{n-1} \lambda Q_v, \tag{6}$$

where σ_w (S m^{-1}) is the water (or aqueous solution) conductivity, β and λ (m^2 s^{-1} V^{-1}) are the effective ion mobility of the counterions contributing to conduction (σ') and polarization (σ''), respectively, Q_v (C m^{-3}) is the excess of charge compensating the surface charge of the solid phase per unit of pore volume, and the exponents m and n are the cementation and the saturation exponents, respectively. The equations of the model do not consider a frequency effect. Q_v is related to the cation exchange capacity (CEC) as follows (Revil & Leroy, 2004),

$$Q_v = \frac{1-\phi}{\phi} \rho \, \text{CEC}. \tag{7}$$

The porosity and water saturation are given by image processing. The water conductivity comes from the geochemical simulation.

Using EIDORS (Electrical Impedance and Diffuse Optical tomography Reconstruction Software), the channel, calcite, and electrodes are meshed (Adler & Lionheart, 2006). The simulated electric current streamlines are straight and parallel to the channel (see Figure S1 in Supporting Information S1). This highlights the relatively minor influence of the calcite sample on the trajectory of the streamlines in comparison with the geometry of the confined channel. Thus, the cementation exponent is fixed at $m = 1$ (Glover, 2009). The saturation exponent is fixed to the standard value $n = 2$ (Ellis & Singer, 2007; Glover, 2017).

The dissolution of calcite ($CaCO_3$) consumes injected protons (H^+) and produces calcium ions (Ca^{2+}) leached in bulk water (S. Li et al., 2016). The chemical reaction is written as follows,

$$CaCO_3 + 2H^+ \rightarrow Ca^{2+} + CO_2 + H_2O. \tag{8}$$

We assume Ca^{2+} and H^+ are the only counterions in the calcite sample EDL. In bulk water, the ion mobilities of ions decrease as salinity increases because of the mutual interaction of cations and anions (Bernard et al., 1992; Leroy et al., 2015). However, this is not the case in the EDL because it contains mostly counterions with the same sign. In addition, we do not expect a drastic change in bulk water composition during the experiment. Therefore, during the calcite dissolution experiment, a drastic change of ion mobilities β and λ values associated with counterions displacement in the EDL is not expected. Thus, the ion mobility β is fixed as the mean value of hydrogen and calcium mobilities (β_{H^+} and $\beta_{Ca^{2+}}$). According to the literature (McCleskey et al., 2012), the non-ideal character of an electrolyte solution can be accounted for by using activity coefficients of hydrogen and calcium cations, γ_{H^+} and $\gamma_{Ca^{2+}}$, as correction factors of the ion limiting mobilities, $\beta^0_{H^+}$ and $\beta^0_{Ca^{2+}}$. Thus,

$$\beta = \frac{1}{2}\left(\gamma_{H^+} \beta^0_{H^+} + \gamma_{Ca^{2+}} \beta^0_{Ca^{2+}}\right). \tag{9}$$

Activity coefficients are calculated by the geochemical simulation, yielding values of $\gamma_{H^+} = 0.967 \pm 0.005$ and $\gamma_{Ca^{2+}} = 0.738 \pm 0.011$. They exhibit low variations and are thus considered constant. The limiting ion mobilities of hydrogen and calcium cations are calculated based on the phreeqc.dat database (Parkhurst & Appelo, 2013) giving $\beta^0_{H^+} = 36.63\ 10^{-8}$ m^2 s^{-1} V^{-1} and $\beta^0_{Ca^{2+}} = 6.24\ 10^{-8}$ m^2 s^{-1} V^{-1}. Thus, it yields $\beta = 19.98\ 10^{-8}$ m^2 s^{-1} V^{-1}. From this, the other ion mobility term λ is also considered constant and fixed as a ratio of β ($\lambda = \beta/\alpha$ with $\alpha > 1$), meaning that the same type of counterions contribute to conduction and polarization (Leroy et al., 2013). Several studies have determined different values for the α ratio, see Leroy et al. (2015) for a review. After testing several values, we have fixed $\alpha = 6$, an intermediate value comprised between 1.6 and 10, the range found in the literature for various minerals (Leroy et al., 2015; Leroy, Li, et al., 2017; Leroy, Weigand, et al., 2017; Ricci et al., 2013). At this stage, there is no distinction between the contribution of the Stern layer and the contribution of the diffuse layer to the complex conductivity. However, we can assume that the contribution is mostly from the Stern layer of calcite, which is very strong according to S. Li et al. (2016).

The CEC is the only fitting parameter. Its value is determined to minimize the residuals r on both components σ' and σ'' such as

$$r(\mathrm{CEC}, t) = |\sigma'_{mod}(\mathrm{CEC}, t) - \sigma'_{dat}(t)| + \alpha\, |\sigma''_{mod}(\mathrm{CEC}, t) - \sigma''_{dat}(t)|, \tag{10}$$

where the subscripts *mod* and *dat* correspond to the modeled and experimental data, respectively. Note that the ratio α, fixed between the ion mobilities β and λ, is used to weight equivalently the two components of the complex conductivity. Maps of the values of the residuals for each component and the minimal values are plotted (Figure S2 in Supporting Information S1). The fitted CEC variations are then smoothed using a first-order Savitzky-Golay filter and applied to get the modeled curves of both components. To estimate the accuracy of the modeled complex electrical conductivity components with the experimental data, the mean absolute error (MAE) is calculated as follows

$$\mathrm{MAE} = \frac{1}{N}\sum |x_{dat}(t) - x_{mod}(t)|, \tag{11}$$

where N is the number of data, x_{dat} the experimental measurements (σ'_{dat} or σ''_{dat}), and x_{mod} the values from the model (σ'_{mod} or σ''_{mod}). The curves of the residuals of each component, which serve to calculate their respective MAE are plotted (Figure S2 in Supporting Information S1).

3. Results and Discussion

This section presents and discusses the modeling results obtained for the coupled workflow. Image processing results are presented first, followed by geochemical simulation and then petrophysical modeling. The section concludes with a discussion of the variations in the adjusted CEC compared to the specific surface area obtained by image processing.

The time variations of porosity ϕ and water saturation S_w obtained from image processing are shown in Figure 3a (Data Set S1 in Supporting Information S1). ϕ shows a monotonic increase toward the maximum value of 1 as calcite is entirely dissolved. The initial value is 0.7, which is high compared to natural carbonate rocks with porosity of ≈ 0.2 (S. Li et al., 2016), but consistent with a quasi 2D microfluidic model (Soulaine et al., 2017). Water saturation shows a more complex behavior. Initially, it is at the maximum value because there is no gas phase in the channel (Figure 2b). At time $t = 0.26$ hr, S_w decreases due to the nucleation of CO_2 bubbles. The S_w negative slope gradually reduces and becomes relatively stable. At the time $t = 4.26$ hr, S_w jumps to its final value of 0.9 because the bubbles are suddenly carried away from the calcite grain. The final value is not maximal because small bubbles remain in the channel. Videos of the calcite dissolution and the segmented images of the bubbles are available Movies S1 and S2.

The porosity and water conductivity obtained from the geochemical simulation performed for fully saturated conditions in the first 13 min of the experiment are plotted in Figure 3a. The porosity exhibits a trend consistent with that obtained from image processing. Indeed, after 13 min of dissolution, the porosity values are 0.72 from the geochemical simulation and 0.73 from the image processing. The water conductivity σ_w corresponds to the calculated value obtained in reservoir BR3 (Figure 2e). The results suggest that σ_w increases rapidly with time because of the small proportion of an inlet acid solution that does not react with calcite. This result correlates with the modeled pH reaching 2.5 in BR3, while the pH of the inlet acid solution was measured at 2.3 (Data Set S2 in Supporting Information S1). The acidic character of the solution corresponds to the major contribution of the H^+ protons to σ_w. After 13 min of dissolution, σ_w is set to increase linearly and reaches the conductivity of the inlet acid solution σ_{HCl} for the final value due to total calcite dissolution.

The measured complex electrical conductivity components σ' and σ'' are represented at the frequency $f = 2.5$ Hz in Figure 3b and c (black squares). This frequency is used because of its low value of the same order of magnitude as the frequencies used to acquire induced polarization measurements in the field (Mendieta et al., 2021). In addition, at this frequency, measurements are not strongly influenced by low-frequency measuring electrode polarization effect nor by high-frequency measuring electrode contact impedance and electromagnetic coupling effects (Huisman et al., 2016). The entire data set is presented in Rembert, Stolz, et al. (2023). Here we only summarize the necessary information for intelligible reading. The complex electrical conductivity components

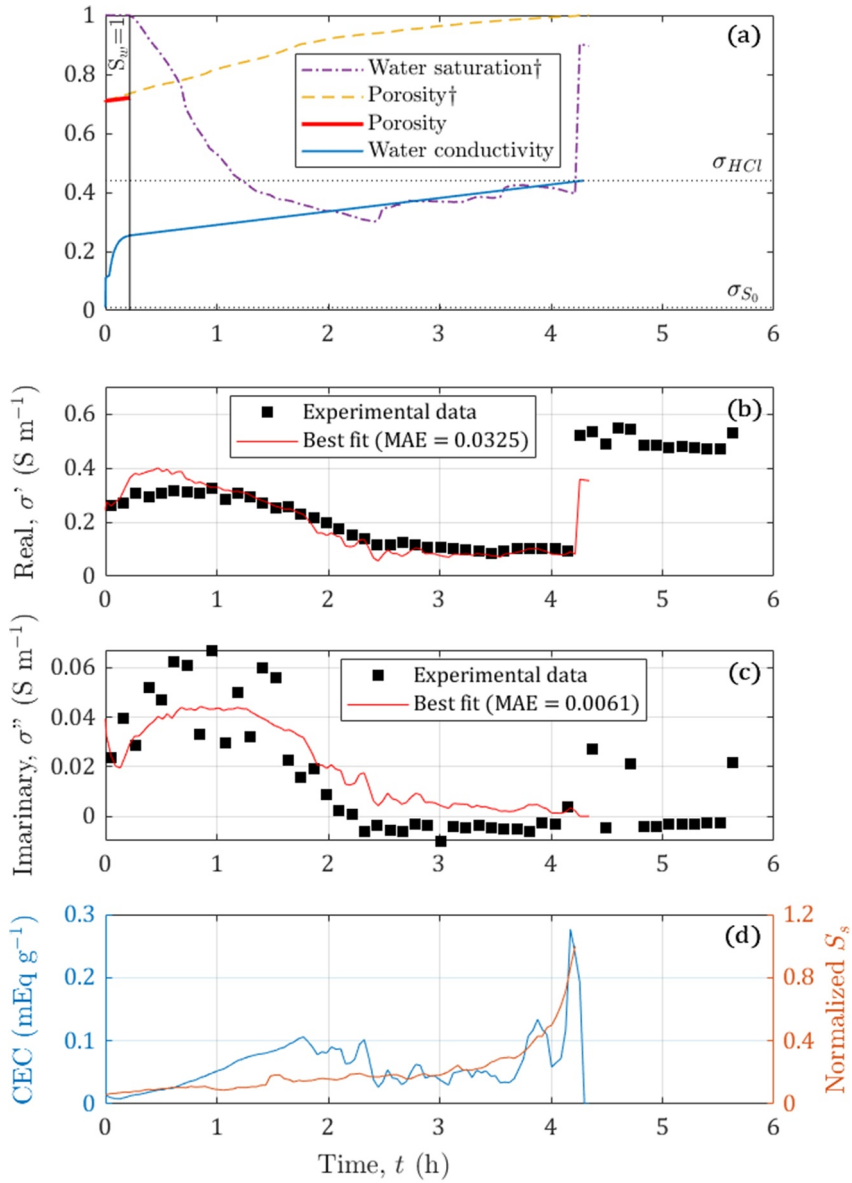

Figure 3. (a) Time evolution of the porosity and the water saturation obtained from the image processing (†), and the porosity and water conductivity obtained from geochemical modeling in fully-saturated conditions. Water conductivity is extrapolated for later times assuming a linear increase reaching the electrical conductivity value of the inlet acid solution σ_{HCl} at the end of the experiment (b, c) Results of the modeling of the real and imaginary components of the complex electrical conductivity. The black squares are the measurements at 2.5 Hz and the red curves are the model results. (d) The fitted CEC and the normalized specific surface area S_s obtained from image processing.

increase first due to calcite dissolution which increases the pore volume and the electrical conductivity of the electrolyte and due to surface roughness modification, which influences EDL polarization. Then, the SIP components decrease after 1 hour of dissolution, when water saturation is dramatically reduced, the bubbles seem to not contribute to polarization. Then, both components start stabilizing at 2.45 hr to a low σ' value (≈ 0.1 S m^{-1}) and close to zero for σ'' (with values even slightly negative). Hangings on σ' are common with S_w curve. Then, at time $t = 4.26$ hr, σ' simultaneous with S_w jumps to a higher final value due to the abrupt detachment of the bubbles in the channel. On the contrary, σ'' remains globally close to zero, since no more polarizable calcite is available in the channel. The red curves in Figures 3b and 3c represent the model results for each component (Data Set S3 in Supporting Information S1). The low MAE values Equation 11, displayed in Figure 3, demonstrate the good agreement between the model and the measurements.

The fitted CEC and the specific surface area normalized by its maximum value are displayed Figure 3d (Data Set S3 in Supporting Information S1). The specific surface area shows a low order of magnitude compared to expected values from the literature ranging between $4 m^2\ g^{-1}$ and $30\ m^2\ g^{-1}$(Bang et al., 2012; Noiriel et al., 2009). This comes from the visualization of the calcite sample from the top and the approximation of the surface roughness from its contour detection. Thus, we present the normalized curve to highlight its global trend exhibiting a linear increase that goes exponential at the end until total dissolution.

The CEC presents remarkable time variations. Initially, it inches up with a smooth and gentle slope which gets steeper at time $t = 0.64$ hr, and reaches 0.1 mEq g^{-1} at time $t = 1.78$ hr. Then, the CEC decreases and oscillates around 0.04 mEq g^{-1}. Finally, at time $t = 3.62$ hr, it increases and reaches the maximal final value of 0.28 mEq g^{-1} before dropping to zero after the complete calcite dissolution. Most of the CEC values range between 0.01 and 0.11 mEq g^{-1}. This range is consistent when studying calcite, for which CEC is reported to fall between 0.001 and 0.211 mEq g^{-1} in the literature (Dohrmann & Kaufhold, 2009; Groenendijk & van Wunnik, 2021). The final maximum value of 0.28 mEq g^{-1} is relatively high but closely aligns with the range for calcite CEC. This increase is consistent with the size reduction of the calcite sample (Ivanić et al., 2020). This finding supports the modeling approach consistency. However, the compliance of Equation 7 is questionable since it applies to the CEC of clays at pH = 7, while calcite buffers pH to 9, which is known to overstep the measurement, and here we have low pH values. In their review, Dohrmann and Kaufhold (2009) emphasize that "pH cannot be regarded as the only controlling parameter" when estimating the CEC and that the "comparability of results" is the major goal.

The global CEC trend is similar to the normalized specific surface area S_s obtained from image processing. This is a remarkable and consistent result, given the relationship $CEC = -Q_0\ S_s$, where Q_0 ($C\ m^{-2}$) is the surface charge density of the calcite mineral, showing that Q_0 is relatively stable with time. However, the geochemical simulation predicts the water conductivity increase and pH decrease, which are known to affect the surface potential of the mineral (Heberling et al., 2021; Skold et al., 2011). Nevertheless, it should be noted that the ranges of water conductivity and pH variations are limited, and thus their effect on polarization is similarly constrained. In addition, the produced CO_2 bubbles dramatically affect the system by decreasing water saturation. However, we assume they do not contribute to polarization because of their smaller specific surface area and weaker surface charge than calcite (Leroy et al., 2012). In addition, most ions except H^+ are repulsed from the bubble/water interface (Leroy et al., 2010). These interesting results will be confronted in the future with more sophisticated modeling approaches based on the description of the evolution of the structure and chemical composition of the calcite/solution interface for further physics-based interpretation.

This modeling has some limitations that open future perspectives. First, while the discussion of the CEC shows consistent results with the literature, the data set used for the modeling is unique, thus, no further comparison can be achieved. Nevertheless, this experiment explores a complex reactive system in partially saturated conditions, applicable to many areas. Therefore, the developed dedicated workflow has capabilities that can be expanded to other systems. However, the geochemical simulation and the petrophysical modeling are currently relatively simplistic, especially for further consideration of the CO_2 bubbles, which are only accounted for in the water saturation term through image processing. Considering CO_2 bubbles effect would help in addressing the frequency effect on the SIP measurements. The current ambition of the geochemical simulation was to provide information for petrophysical modeling. In the future, the petrophysical model should become more sophisticated, then, it will be necessary to incorporate more complexity into the geochemical simulation. Using dedicated reactive-transport calculation code (e.g., CrunchFlow, CrunchTope, porousMedia4Foam) for a more realistic description of the system represents a promising advancement in the understanding of the system at the pore scale (e.g., Deng et al., 2021; Soulaine et al., 2021; Steefel & Molins, 2009).

4. Conclusions

We have developed a numerical approach coupling image processing, geochemical simulation, and petrophysical modeling. We use it to interpret a unique data set of calcite dissolution monitoring performed at the microscale with SIP and microscope images. The study uses the equivalent circuit model. Despite its phenomenological foundation, this model allows for the sober use of fitting parameters and highlights the correlation between CEC and specific surface area. The convergence of this model demonstrates that the microscale approach yields results that can be upscaled using geoelectrical monitoring, which provides an averaging response of the micrometric

scale heterogeneity. The outcomes of this methodology are beneficial for the physics-based advancement of pore-scale modeling of complex electrical conductivity. In the future, we intend to investigate the influence of CO_2 bubble generation in greater detail. We plan to develop a more sophisticated hydrodynamic and physicochemical model of the calcite-solution interface to be coupled with a mechanistic numerical modeling framework of the IP signature.

Data Availability Statement

Experimental data of Rembert, Stolz, et al. (2023) were used in the manuscript preparation. Matlab 2022a and the Image Processing Toolbox were employed for image processing and petrophysical modeling. PhreeqC v3 was utilized for geochemical simulation. Supporting Information S1 files are archived on Zenodo (Rembert et al., 2024).

Acknowledgments
Funders are the French National Research Agency (ANR, LabEx VOLTAIRE –Grant ANR-10-LABX-100–01, IMAGE project –Grant ANR-21-CE04-0013) and the European Union (ERC, TRACE-it project Grant n°101039854).

References

Adler, A., & Lionheart, W. R. B. (2006). Uses and abuses of EIDORS: An extensible software base for EIT. *Physiological Measurement*, *27*(5), S25–S42. https://doi.org/10.1088/0967-3334/27/5/S03

Bang, J.-H., Jang, Y. N., Kim, W., Song, K. S., Jeon, C. W., Chae, S. C., et al. (2012). Specific surface area and particle size of calcium carbonate precipitated by carbon dioxide microbubbles. *Chemical Engineering Journal*, *198–199*, 254–260. https://doi.org/10.1016/j.cej.2012.05.081

Bate, B., Cao, J., Zhang, C., & Hao, N. (2021). Spectral induced polarization study on enzyme induced carbonate precipitations: Influences of size and content on stiffness of a fine sand. *Acta Geotechnica*, *16*(3), 841–857. https://doi.org/10.1007/s11440-020-01059-8

Ben Moshe, S., Kessouri, P., Erlich, D., & Furman, A. (2021). Geophysically based analysis of breakthrough curves and ion exchange processes in soil. *Hydrology and Earth System Sciences*, *25*(6), 3041–3052. https://doi.org/10.5194/hess-25-3041-2021

Bernard, O., Kunz, W., Turq, P., & Blum, L. (1992). Self-diffusion in electrolyte solutions using the mean spherical approximation. *Journal of Physical Chemistry*, *96*(1), 398–403. https://doi.org/10.1021/j100180a074

Binley, A., & Kemna, A. (2005). DC resistivity and induced polarization methods. In Y. Rubin & S. S. Hubbard (Eds.), *Hydrogeophysics* (pp. 129–156). Springer Netherlands. https://doi.org/10.1007/1-4020-3102-5_5

Binley, A., & Slater, L. (2020). *Resistivity and induced polarization: Theory and applications to the near-surface earth*. Cambridge University Press.

Blanc, P., Lassin, A., Piantone, P., Azaroual, M., Jacquemet, N., Fabbri, A., & Gaucher, E. C. (2012). Thermoddem: A geochemical database focused on low temperature water/rock interactions and waste materials. *Applied Geochemistry*, *27*(10), 2107–2116. https://doi.org/10.1016/j.apgeochem.2012.06.002

Deng, H., Tournassat, C., Molins, S., Claret, F., & Steefel, C. (2021). A pore-scale investigation of mineral precipitation driven diffusivity change at the column-scale. *Water Resources Research*, *57*(5), e2020WR028483. https://doi.org/10.1029/2020WR028483

Dohrmann, R., & Kaufhold, S. (2009). Three new, quick CEC methods for determining the amounts of exchangeable calcium cations in calcareous clays. *Clays and Clay Minerals*, *57*(3), 338–352. https://doi.org/10.1346/CCMN.2009.0570306

Ellis, D. V., & Singer, J. M. (2007). *Well logging for earth scientists* (Vol. 692). Springer.

Glover, P. W. J. (2009). What is the cementation exponent? A new interpretation. *The Leading Edge*, *28*(1), 82–85. https://doi.org/10.1190/1.3064150

Glover, P. W. J. (2017). A new theoretical interpretation of Archie's saturation exponent. *Solid Earth*, *8*(4), 805–816. https://doi.org/10.5194/se-8-805-2017

Groenendijk, D. J., & van Wunnik, J. N. M. (2021). Surfactant adsorption and ion exchange on calcite surfaces. *Energy & Fuels*, *35*(10), 8763–8772. https://doi.org/10.1021/acs.energyfuels.1c00670

Halisch, M., Hupfer, S., Weller, A., Dlugosch, R., & Plumhoff, H.-P. (2018). An experimental setup for the assessment of effects of carbonate rock dissolution on complex electrical conductivity spectra. *Proceedings of core symposium* (Vol. 9).

Heberling, F., Klačić, T., Raiteri, P., Gale, J. D., Eng, P. J., Stubbs, J. E., et al. (2021). Structure and surface complexation at the calcite(104)–water interface. *Environmental Science & Technology*, *55*(18), 12403–12413. https://doi.org/10.1021/acs.est.1c03578

Huisman, J. A., Zimmermann, E., Esser, O., Haegel, F.-H., Treichel, A., & Vereecken, H. (2016). Evaluation of a novel correction procedure to remove electrode impedance effects from broadband sip measurements. *Journal of Applied Geophysics*, *135*, 466–473. https://doi.org/10.1016/j.jappgeo.2015.11.008

Ivanić, M., Durn, G., Škapin, S. D., & Sondi, I. (2020). Size-related mineralogical and surface physicochemical properties of the mineral particles from the recent sediments of the eastern Adriatic Sea. *Chemosphere*, *249*, 126531. https://doi.org/10.1016/j.chemosphere.2020.126531

Kemna, A., Binley, A., Cassiani, G., Niederleithinger, E., Revil, A., Slater, L., et al. (2012). An overview of the spectral induced polarization method for near-surface applications. *Near Surface Geophysics*, *10*(6), 453–468. https://doi.org/10.3997/1873-0604.2012027

Koohbor, B., Deparis, J., Leroy, P., Ataie-Ashtiani, B., Davarzani, H., & Colombano, S. (2022). DNAPL flow and complex electrical resistivity evolution in saturated porous media: A coupled numerical simulation. *Journal of Contaminant Hydrology*, *248*, 104003. https://doi.org/10.1016/j.jconhyd.2022.104003

Laloy, E., Javaux, M., Vanclooster, M., Roisin, C., & Bielders, C. L. (2011). Electrical resistivity in a loamy soil: Identification of the appropriate pedo-electrical model. *Vadose Zone Journal*, *10*(3), 1023–1033. https://doi.org/10.2136/vzj2010.0095

Lee, J. N., Park, C., & Whitesides, G. M. (2003). Solvent compatibility of poly(dimethylsiloxane)-based microfluidic devices. *Analytical Chemistry*, *75*(23), 6544–6554. https://doi.org/10.1021/ac0346712

Leroy, P., Devau, A., Revil, N., & Bizi, M. (2013). Influence of surface conductivity on the apparent zeta potential of amorphous silica nanoparticles. *Journal of Colloid and Interface Science*, *410*(1), 81–93. https://doi.org/10.1016/j.jcis.2013.08.012

Leroy, P., Jougnot, D., Revil, A., Lassin, A., & Azaroual, M. (2012). A double layer model of the gas bubble/water interface. *Journal of Colloid and Interface Science*, *388*(1), 243–256. https://doi.org/10.1016/j.jcis.2012.07.029

Leroy, P., Lassin, A., Azaroual, M., & Andre, L. (2010). Predicting the surface tension of aqueous 1:1 electrolyte solutions at high salinity. *Geochimica et Cosmochimica Acta*, *74*(19), 5427–5442. https://doi.org/10.1016/j.gca.2010.06.012

Leroy, P., Li, S., Jougnot, D., Revil, A., & Wu, Y. (2017a). Modeling the evolution of complex conductivity during calcite precipitation on glass beads. *Geophysical Journal International*, *209*(1), 123–140. https://doi.org/10.1093/gji/ggx001

Leroy, P., Tournassat, C., Bernard, O., Devau, N., & Azaroual, M. (2015). The electrophoretic mobility of montmorillonite. zeta potential and surface conductivity effects. *Journal of Colloid and Interface Science*, *451*(1), 21–39. https://doi.org/10.1016/j.jcis.2015.03.047

Leroy, P., Weigand, M., Mériguet, G., Zimmermann, E., Tournassat, C., Fagerlund, F., et al. (2017b). Spectral induced polarization of Na-montmorillonite dispersions. *Journal of Colloid and Interface Science*, *505*, 1093–1110. https://doi.org/10.1016/j.jcis.2017.06.071

Li, H., Wang, F., Wang, Y., Yuan, Y., Feng, G., Tian, H., & Xu, T. (2023). Phase-field modeling of coupled reactive transport and pore structure evolution due to mineral dissolution in porous media. *Journal of Hydrology*, *619*, 129363. https://doi.org/10.1016/j.jhydrol.2023.129363

Li, S., Leroy, P., Heberling, F., Devau, N., Jougnot, D., & Chiaberge, C. (2016). Influence of surface conductivity on the apparent zeta potential of calcite. *Journal of Colloid and Interface Science*, *468*, 262–275. https://doi.org/10.1016/j.jcis.2016.01.075

Mansouri-Boroujeni, M., Soulaine, C., Azaroual, M., & Roman, S. (2023). How interfacial dynamics controls drainage pore-invasion patterns in porous media. *Advances in Water Resources*, *171*, 104353. https://doi.org/10.1016/j.advwatres.2022.104353

McCleskey, R. B., Nordstrom, D. K., & Ryan, J. N. (2012). Comparison of electrical conductivity calculation methods for natural waters. *Limnology and Oceanography: Methods*, *10*(11), 952–967. https://doi.org/10.4319/lom.2012.10.952

Mendieta, A., Jougnot, D., Leroy, P., & Maineult, A. (2021). Spectral induced polarization characterization of non-consolidated clays for varying salinities—An experimental study. *Journal of Geophysical Research: Solid Earth*, *126*(4), e2020JB021125. https://doi.org/10.1029/2020JB021125

Noiriel, C., Luquot, L., Madé, B., Raimbault, L., Gouze, P., & van der Lee, J. (2009). Changes in reactive surface area during limestone dissolution: An experimental and modelling study. *Chemical Geology*, *265*(1), 160–170. https://doi.org/10.1016/j.chemgeo.2009.01.032

Norouzisadeh, M., Leroy, P., & Soulaine, C. (2024). A lubrication model with slope-dependent disjoining pressure for modeling wettability alteration. *Computer Physics Communications*, *298*, 109114. https://doi.org/10.1016/j.cpc.2024.109114

Osselin, F., Kondratiuk, P., Budek, A., Cybulski, O., Garstecki, P., & Szymczak, P. (2016). Microfluidic observation of the onset of reactive-infiltration instability in an analog fracture. *Geophysical Research Letters*, *43*(13), 6907–6915. https://doi.org/10.1002/2016GL069261

Parkhurst, D. L., & Appelo, C. A. J. (2013). *Description of input and examples for PHREEQC version 3: A computer program for speciation, batch-reaction, one-dimensional transport, and inverse geochemical calculations (tech. rep. no. 6-A43)*. US Geological Survey. https://doi.org/10.3133/tm6A43

Poonoosamy, J., Soulaine, C., Burmeister, A., Deissmann, G., Bosbach, D., & Roman, S. (2020). Microfluidic flow-through reactor and 3D Raman imaging for *in situ* assessment of mineral reactivity in porous and fractured porous media. *Lab on a Chip*, *20*(14), 2562–2571. https://doi.org/10.1039/D0LC00360C

Rahmani, A., Franz, M., Bär, F., Backes, C., Byrne, J. M., & Mellage, A. (2024). Changing Cr-retention capacity of magnetite-coated sand captured by spectral induced polarization (SIP). *ACS ES&T Water*, *4*(5), 2181–2191. https://doi.org/10.1021/acsestwater.3c00824

Rembert, F., Jougnot, D., & Guarracino, L. (2020). A fractal model for the electrical conductivity of water-saturated porous media during mineral precipitation-dissolution processes. *Advances in Water Resources*, *145*, 103742. https://doi.org/10.1016/j.advwatres.2020.103742

Rembert, F., Jougnot, D., Luquot, L., & Guérin, R. (2022). Interpreting self-potential signal during reactive transport: Application to calcite dissolution and precipitation. *Water*, *14*(10), 1632. https://doi.org/10.3390/w14101632

Rembert, F., Léger, M., Jougnot, D., & Luquot, L. (2023). Geoelectrical and hydro-chemical monitoring of karst formation at the laboratory scale. *Hydrology and Earth System Sciences*, *27*(2), 417–430. https://doi.org/10.5194/hess-27-417-2023

Rembert, F., Leroy, P., Lassin, A., & Roman, S. (2024). Videos of the processed microscope images and time series of the petrophysical parameters from image processing and geochemical simulation and of the measured induced polarisation [dataset]. *Zenodo*. https://doi.org/10.5281/zenodo.14202713

Rembert, F., Stolz, A., Soulaine, C., & Roman, S. (2023). A microfluidic chip equipped for geoelectrical monitoring of the critical zone processes. *Lab on a Chip*, *23*(15), 3433–3442. https://doi.org/10.1039/D3LC00377A

Revil, A., & Florsch, N. (2010). Determination of permeability from spectral induced polarization in granular media. *Geophysical Journal International*, *181*(3), 1480–1498. https://doi.org/10.1111/j.1365-246X.2010.04573.x

Revil, A., Karaoulis, M., Johnson, T., & Kemna, A. (2012). Review: Some low-frequency electrical methods for subsurface characterization and monitoring in hydrogeology. *Hydrogeology Journal*, *20*(4), 617–658. https://doi.org/10.1007/s10040-011-0819-x

Revil, A., & Leroy, P. (2004). Constitutive equations for ionic transport in porous shales. *Journal of Geophysical Research*, *109*(B3), 1–19. https://doi.org/10.1029/2003JB002755

Riazi, M., Sohrabi, M., Bernstone, C., Jamiolahmady, M., & Ireland, S. (2011). Visualisation of mechanisms involved in CO_2 injection and storage in hydrocarbon reservoirs and water-bearing aquifers. *Chemical Engineering Research and Design*, *89*(9), 1827–1840. https://doi.org/10.1016/j.cherd.2011.03.009

Ricci, M., Spijker, P., Stellacci, F., Molinari, J. F., & Voitchovsky, K. (2013). Direct visualization of single ions in the Stern layer of calcite. *Langmuir*, *29*(7), 2207–2216. https://doi.org/10.1021/La3044736

Roman, S., Soulaine, C., Al Saud, M. A., Kovscek, A., & Tchelepi, H. (2016). Particle velocimetry analysis of immiscible two-phase flow in micromodels. *Advances in Water Resources*, *95*, 199–211. https://doi.org/10.1016/j.advwatres.2015.08.015

Roman, S., Soulaine, C., & Kovscek, A. R. (2020). Pore-scale visualization and characterization of viscous dissipation in porous media. *Journal of Colloid and Interface Science*, *558*, 269–279. https://doi.org/10.1016/j.jcis.2019.09.072

Skold, M., Revil, A., & Vaudelet, P. (2011). The pH dependence of spectral induced polarization of silica sands: Experiment and modeling. *Geophysical Research Letters*, *38*(12). https://doi.org/10.1029/2011GL047748

Song, W., de Haas, T. W., Fadaei, H., & Sinton, D. (2014). Chip-off-the-old-rock: The study of reservoir-relevant geological processes with real-rock micromodels. *Lab on a Chip*, *14*(22), 4382–4390. https://doi.org/10.1039/C4LC00608A

Soulaine, C. (2024). Micro-continuum modeling: An hybrid-scale approach for solving coupled processes in porous media. *Water Resources Research*, *60*(2), e2023WR035908. https://doi.org/10.1029/2023WR035908

Soulaine, C., Pavuluri, S., Claret, F., & Tournassat, C. (2021). porousmedia4foam: Multi-scale open-source platform for hydro-geochemical simulations with OpenFOAM®. *Environmental Modelling and Software*, *145*, 105199. https://doi.org/10.1016/j.envsoft.2021.105199

Soulaine, C., & Roman, S. (2022). La microfluidique infiltre les géosciences. *Pour la Science*, *535*(5), 50–58. https://doi.org/10.3917/pls.535.0050

Soulaine, C., Roman, S., Kovscek, A., & Tchelepi, H. A. (2017). Mineral dissolution and wormholing from a pore-scale perspective. *Journal of Fluid Mechanics*, *827*, 457–483. https://doi.org/10.1017/jfm.2017.499

Soulaine, C., Roman, S., Kovscek, A., & Tchelepi, H. A. (2018). Pore-scale modelling of multiphase reactive flow: Application to mineral dissolution with production of CO_2. *Journal of Fluid Mechanics*, *855*, 616–645. https://doi.org/10.1017/jfm.2018.655

Steefel, C. I., & Molins, S. (2009). Crunchflow. Software for modeling multicomponent reactive flow and transport. *User's manual*, 12–91.

Tarasov, A., & Titov, K. (2013). On the use of the Cole–Cole equations in spectral induced polarization. *Geophysical Journal International*, *195*(1), 352–356. https://doi.org/10.1093/gji/ggt251

Vinegar, H. J., & Waxman, M. H. (1984). Induced polarization of shaly sands. *Geophysics*, *49*(8), 1267–1287. https://doi.org/10.1190/1.1441755

Waxman, M., & Smits, L. (1968). Electrical conductivities in oil-bearing shaly sands. *Society of Petroleum Engineers Journal*, *8*(02), 107–122. https://doi.org/10.2118/1863-A

Yun, W., Ross, C., Roman, S., & Kovscek, A. (2017). Creation of a dual-porosity and dual-depth micromodel for the study of multiphase flow in complex porous media. *Lab on a Chip*, *17*(8), 1462–1474. https://doi.org/10.1039/C6LC01343K

Zarif, F., Kessouri, P., & Slater, L. (2017). Recommendations for field-scale induced polarization (IP) data acquisition and interpretation. *Journal of Environmental & Engineering Geophysics*, *22*(4), 395–410. https://doi.org/10.2113/jeeg22.4.395